CHAPTER 4

A model for early diagenetic processes in sediments of the continental shelf of the Black Sea

J.W.M. Wijsman, P.M.J. Herman, J.J. Middelburg and K. Soetaert
Accepted for publication in *Estuarine, Coastal and Shelf Science*

Introduction

The river Danube is a major source of organic matter and nutrients for the Black Sea (Popa, 1993), increasing the primary production on the shelf. The enhanced rates of benthic mineralization following the deposition of the plankton material, in combination with a pronounced stratification of the water column in the summer period, may result in anoxic or hypoxic bottom waters. As a result, mass mortality among the benthic community is frequently observed in the coastal zone of the Black Sea continental shelf (Tolmazin, 1985b). Seasonal depletion of oxygen contents in the near bottom waters have been reported for various coastal systems (Harper et al., 1981; Faganeli et al., 1985). In general oxygen depletion events are limited to the summer periods when the water column is stratified. Movement of the chemocline by (wind-induced) upwellings or internal waves can be an additional source for anoxic bottom water on the continental shelf of the Black Sea (Kempe et al., 1990).

The low oxygen concentration of the bottom water and the high rates of organic matter sedimentation increase the importance of the anaerobic degradation processes in the sediment. Hydrogen sulfide, which may be toxic for many benthic organisms, is produced by sulfate reduction in the sediment when the more favorable electron acceptors such as oxygen, nitrate, manganese oxides and iron oxides are exhausted (Froelich et al., 1979). The hydrogen sulfide may react with iron to form iron sulfides such as FeS and FeS_2. As such, iron may buffer the release of free sulfide. Larger rivers are a major source of reactive iron for continental shelf systems (Aller et al., 1986; Canfield, 1989b). Although iron and sulfur cycling has been studied in sediments of the Black Sea (Calvert and Karlin, 1991; Lyons and Berner, 1992; Lyons et al., 1993; Lyons, 1997), there are no data on the northwestern shelf sediments, that receive significant quantities of reactive iron from the Danube.

Diagenetic models can be used as a tool to study diagenetic processes in the sediments. Recent development in diagenetic modeling resulted in a complex description of multiple reaction pathways with a high degree of interaction between

the acting species, *pH* dependence and non-linear reaction kinetics (Boudreau, 1991; Rabouille and Gaillard, 1991a; Boudreau and Canfield, 1993; Cai et al., 1995; Van Cappellen and Wang, 1995; Boudreau, 1996a, Dhakar and Burdige, 1996; Soetaert et al., 1996a; Soetaert et al., 1996b; Van Cappellen and Wang, 1996; Wang and Van Cappellen, 1996). The development of these complex models was facilitated by the availability of more powerful computer hardware and advanced numerical methods (Steefel and MacQuarrie, 1996). Especially the models of Boudreau (1996a), Van Cappellen & Wang (1995; 1996) and Wang & Van Cappellen (1996) provided an extensive description of the iron and sulfur chemistry in sediments. Their models include the description of alkalinity conservation in the pore water, which determines the *pH*.

In this paper we present a model for early diagenetic processes in the sediments of the Black Sea. The *pH* in this model is introduced as a forcing function and is not determined by the concentrations of all the other species. The obtained reduction of the number of state variables makes the model easier to interpret and minimizes computing time, so that extensive sensitivity analysis could be performed. The model is capable to generate steady state profiles as well as to run dynamic simulations. The present model is an extension of the model of Soetaert et al. (1996a), which was constructed for a range of marine systems. Since they where mainly interested in organic carbon, oxygen and nitrogen they lumped the anoxic mineralization processes, including manganese reduction, iron reduction, sulfate reduction and methanogenesis together. The reduced substances (Mn^{2+}, Fe^{2+}, H_2S and CH_4) were represented as one pool of oxygen demand units (Soetaert et al., 1996a; Soetaert et al., 1996b). Since we were especially interested in the interaction between the sulfur and iron cycling in the sediment, we extended the model with an explicit description of the anaerobic mineralization (manganese reduction, iron reduction, sulfate reduction and methanogenesis) and re-oxidation processes. The model will be applied to a station on the northwestern shelf of the Black Sea and its performance will be discussed.

Material and methods

The output of the model will be compared to data from station 9 of the 49th cruise of the Prof. Vodyanitsky in May 1997. This station at a water depth of 57 m was located 44°34' North and 29°46' East just in front of the Danube delta (Figure 4.1). The temperature of the bottom water at the time of sampling was 5.8°C. This station has been selected because a rather complete set of data was available and depth profiles of iron and sulfur components indicated that it comprised iron and sulfate reducing layers.

Shipboard procedures

Sediment was recovered with a Reineck box-corer ($60 \times 30 \times 30$ cm) and was sub-sampled with Plexiglas core tubes (10.3 cm inner diameter, 50 cm length). The cores were sectioned in several depth intervals 0–0.5, 0.5–1, 1–2, 2–3, 3–4, 4–5, 5–7, 7–9, 9–11, 14–16, 19–21 and 24–26 cm under a nitrogen atmosphere (O_2-concentration < 0.05 %) in a glove box. The pore water was collected by squeezing the sediment over a 0.45 µm filter with a small (< 1 bar) overpressure of nitrogen gas.
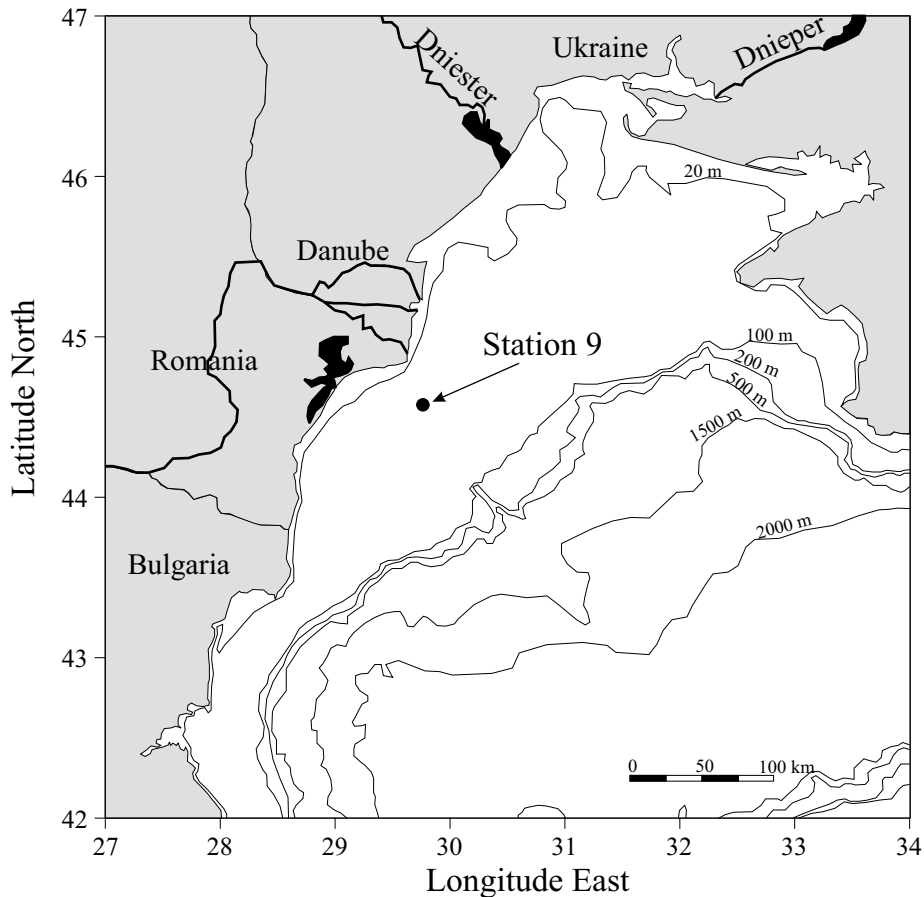
Figure 4.1. Location of station 9 on the northwestern continental shelf of the Black Sea

A sub-sample of 3 ml pore water was collected in 10 ml headspace vials, capped and acidified with 20% H_2SO_4. A second sub-sample of 1 ml was put into an eppendorf vial to which 50 µl of $Zn(Ac)_2$ (20%) was added. The rest of the pore water was stored in 20 ml PVC bottles and sealed in diffusion-free bags to prevent oxygen contamination of the samples. The remainder of the sediment after squeezing was collected in 20 ml glass vials and sealed in diffusion-free bags under nitrogen atmosphere. All samples were removed from the glove box and stored at 4°C (headspace vials) or frozen (PVC bottles, eppendorf vials and sediment samples).

Additional sediment was sub-sampled from the box-corer with Plexiglas core tubes (5.8 cm inner diameter, 50 cm length) for organic carbon content and porosity analysis. The cores were sectioned in several depth intervals 0–0.5, 0.5–1, 1–1.5, 1,5–2, 2–3, 3–4, 4–5, 5–7, 7–9, 9–11, 14–16, 19–21 and 24–26 cm. Care was taken that no pore water was lost. The sediment was put into 50 ml polycarbonate vials and stored frozen.

Depth profiles of oxygen in the sediment were obtained using Clark style micro-electrodes with guard cathode (Diamond General #737GC) at 0.2 mm resolution. The electrodes had a tip-diameter of 40–60 µm and an output of 300 to 1000 pA at oxygen saturation. The overlying water was continuously refreshed with bottom water at *in situ* temperature to prevent depletion of oxygen during measurement. Depth profiles of *pH* in the sediment with a resolution of 2 mm were obtained with a *pH* micro-electrode.

Laboratory procedures

Dissolved *Fe* and *Mn* were determined in the acidified headspace samples with a Perkin Elmer graphic furnace atomic absorption spectrophotometer equipped with Zeeman background correction. NO_3^-, NO_2, NH_4^+ and SO_4^{2-} were measured using an auto-analyzer. $\Sigma H_2 S$ ($H_2 S$, HS^- and S^{2-}) was determined by spectrophotometry (Cline, 1969).

The sediment from the glass vials was analyzed for iron sulfides (*FeS* and *FeS₂*) and dithionite-extractable iron. Samples were transferred into a Coy anaerobic chamber (Coy Laboratory Products, Ann Arbor, Michigan) with an atmosphere of 5% hydrogen plus 95% nitrogen. Any traces of oxygen were consequently removed by reaction with hydrogen.

Acid Volatile Sulfide (AVS), the sum of free sulfide and *FeS*, was determined by cold acid distillation (Fossing and Jørgensen, 1989). About 0.5 g homogenized wet sediment was put into a 100 ml reaction vessel and acidified with 10 ml de-oxygenated 6.0 N *HCl*. The liberated $H_2 S$ was stripped from the slurry for 2 hours using N_2 as carrier gas and trapped in 10 ml de-oxygenated $Zn(Ac)_2$ (2%). The concentration of *ZnS* in the traps was determined with the methylene-blue method (Cline, 1969).

Pyrite was determined by the chromium reduction method (Zhabina and Volkov, 1978; Canfield et al., 1986). The samples were dried (40°C) and extracted with acetone to remove AVS, organic polysulfides and elemental sulfur (Passier et al., 1996). About 10 mg acetone extracted sediment was put into a 100 ml reaction vessel and degassed for 20 minutes with N_2. Subsequently 16 ml 1 M Cr^{2+} in 0.5 N *HCl* and 8 ml de-oxygenated 12 N *HCl* were added to the sample. The sulfide generated was stripped from the solution for 2 hours and trapped in 10 ml $Zn(Ac)_2$ (2%). The *ZnS* in the traps was measured spectrophotometrically as described above.

Dithionite extractable iron content was determined in duplicate following Kostka & Luther (1994). Ten ml dithionite (sodium dithionite 50 g l^{-1} in 0.2 M sodium citrate / 0.35 M acetic acid *pH*=4.8) was added to 0.5 – 1.0 g wet weight sediment in 20 ml glass vials. The vials were vortex mixed and shaken for 2 hours on a rotary shaker. After extraction, the samples were filtered and stored > 1 day to oxidize the dithionite (Canfield et al., 1993b). Total iron [*Fe*(II) + *Fe*(III)] in the sample was determined with reducing ferrozine. Dithionite is supposed to extract *Fe*(III) from poorly and well crystallized *Fe*-oxides (except magnetite) and *Fe*(II) from AVS and carbonates or adsorbed to sedimentary particles (Canfield, 1989b, Canfield et al., 1993b). The amount of *Fe(OH)₃* in the sediment was estimated by the difference between the dithionite-extractable iron and the iron present in *FeS*.

Water content was calculated from weight loss. The porosity was calculated from the water content assuming a sediment density of 2.55 g cm⁻³. Organic carbon was determined with a Carlo Erba NA 1500 elemental analyzer, after *in situ* hydrochloric acid (25%) acidification to remove the inorganic carbon (Nieuwenhuize et al., 1994).

Chl-*a* was extracted from freeze-dried samples using methanol (95%) buffered with ammonium acetate and sonicated for 10 minutes. The extracts were analyzed for chloropigments by reverse-phase high performance liquid chromatography (RP–HPLC).

Concept of the model

Generalized diagenetic equation

Models for early diagenesis are usually based on the so-called General Diagenetic equation, an Advection–Diffusion–Reaction type of equation (Berner, 1980b; Boudreau, 1997):

$$\frac{\partial \xi C_i}{\partial t} = -\frac{\partial}{\partial x}\left[-\xi D \frac{\partial C_i}{\partial x} + \omega \xi C_i\right] + \sum \xi REAC_i \,, \tag{4.1}$$

where x is sediment depth (cm), t is time (d) and ξC_i is the concentration of species i (in units of mol cm^{-3} bulk sediment). For solute species ξ stands for porosity and for solid components ξ stands for (1-porosity). D is the total dispersion–diffusion coefficient (cm^2 d^{-1}), ω is the advection rate (cm d^{-1}) and $\sum \xi REAC_i$ is the sum of all production/consumption of species i in biogeochemical reactions (mol cm^{-3} bulk sediment d^{-1}). The transport processes included are molecular diffusion and bio-irrigation for solute species, bioturbation for solid components and advection for both solids and solutes.

At the lower boundary concentrations of solid and dissolved components do not change with depth (zero gradient boundary). The upper boundary condition for dissolved components is the bottom water concentration and a deposition flux is imposed for the solid components. The model is able to calculate steady-state profiles as well as to run dynamically under time-variable forcing, using the steady-state concentration profiles as a starting condition.

Biogeochemical processes

State variables

A set of 14 state variables was included in the model (Table 4.1). Concentrations of dissolved species are all expressed in units of μmol L^{-1} pore water and those for solid species in units of μmol dm^{-3} total solids. Since benthic primary production on the Black Sea continental shelf can be neglected, it can be assumed that all the oxygen originates from the water column. In the sediment oxygen is consumed by the degradation of organic matter and the re-oxidation of reduced substances. The flux of oxygen is consequently always directed into the sediment. Nitrate can either be consumed (denitrification) or produced (nitrification) in the sediment. Depending on the relative importance of these processes and the nitrate concentration of the bottom water, there may either be an influx or an outflux of nitrate into the sediment. Sulfate is a major constituent in the seawater and is used as an oxidant for degradation processes by sulfate reducers. The other dissolved species (NH_4^+, Mn^{2+}, Fe^{2+}, ΣH_2S and CH_4) are reduced components that are produced during degradation of organic matter. In general there is an outflux of these components from the sediment. A constant fraction of ammonium is adsorbed to the sediment (Berner, 1980b; Soetaert et al., 1996a). Adsorption of Fe^{2+} and Mn^{2+} to sediment particles (Van Cappellen and Wang, 1996) is not taken into account.

Table 4.1. Dissolved and solid species included in the model. Units of the dissolved species are µmol L^{-1} and units of solid species are µmol dm^{-3}

Solute species	Solid Species
O_2	$(CH_2O)_x(NH_3)_y(H_3PO_4)_{fast}$
NO_3^-	$(CH_2O)_x(NH_3)_y(H_3PO_4)_{slow}$
SO_4^{2-}	MnO_2
NH_4^+	$Fe(OH)_3$
Mn^{2+}	FeS
Fe^{2+}	FeS_2
ΣH_2S	
CH_4	

The model does not resolve sulfide speciation (H_2S, HS^- and S^{2-}). However, this is not necessary because the *pH* is imposed (see below) and the concentrations of these sulfide components can be calculated from the total sulfide (ΣH_2S) concentration. In marine sediments the *pH* is always lower than 12 and the contribution of the sulfide ion (S^{2-}) can therefore be neglected (Goldhaber and Kaplan, 1975). The H_2S concentration at a specific *pH* value is then calculated from the total sulfide concentration ΣH_2S:

$$[H_2S] = \left(1 - \frac{K_1'}{10^{-pH}}\right)^{-1} \cdot [\Sigma H_2S],\qquad(4.2)$$

where the dissociation constant (K_1') is depending on temperature and salinity (Millero, 1986). The remainder of the total sulfide is bisulfide ($HS^- = \Sigma H_2S - H_2S$).

Six solid components are distinguished in the model, including fast and slow decaying organic carbon, represented as $(CH_2O)_x(NH_3)_y(H_3PO_4)_{fast}$ and $(CH_2O)_x(NH_3)_y(H_3PO_4)_{slow}$ respectively. The coefficients *x* and *y* denote molar *C:P* and *N:P* ratios respectively. This organic matter is deposited from the water column and degraded in the sediment. Two metal oxides, manganese oxide (MnO_2) and iron (hydr)oxides ($Fe(OH)_3$) reach the sediment by sedimentation and are formed by oxidation. A fraction of the $Fe(OH)_3$ reaching the sediment is assumed not to be reducible on the timescale relevant for early diagenesis. Iron monosulfide (FeS) and pyrite (FeS_2) are formed by interaction of sulfide and ferrous iron.

An important difference with the models of Boudreau (1996a) and Van Cappellen and Wang (1996) is that the alkalinity conservation equation is not included and it is therefore not possible to model the *pH*-profiles. The *pH* profile was therefore imposed via a fourth-order polynome for a depth less than 8 cm (Figure 4.2). The *pH* was assumed not to change at depths > 8 cm. Imposing rather than modeling sediment *pH* not only simplifies the model and significantly reduces computing time, but also reduces uncertainty in modeling *pH* dependent processes. Minimization of computing time is a requirement for coupling with water column biogeochemical models. Our understanding of the factors controlling sedimentary *pH* values is rather incomplete so that models are not yet able to accurately produce *pH* profiles (Boudreau, 1996a; Van Cappellen and Wang, 1996; Meysman, pers. Comm. 1999).
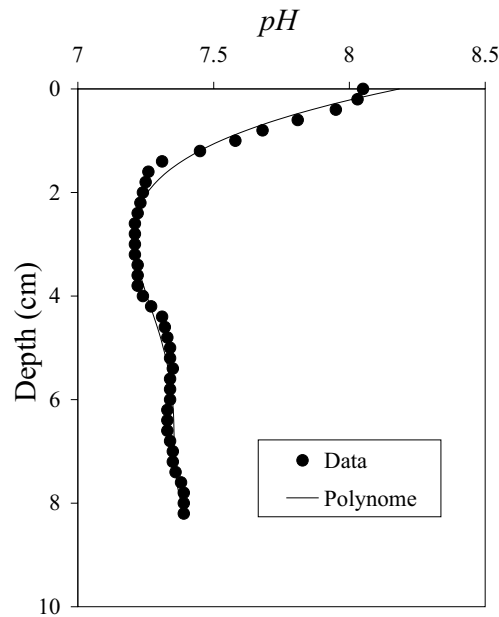
Figure 4.2. *pH* versus depth. A fourth-order polynome (solid line) was fitted through the measured data (dots). This polynome was used as a forcing function for the model

Mineralization reactions

The degradation of organic matter is an oxidative process that requires an electron acceptor. The sequence in which the electron acceptors are utilized is determined by the inhibition of various oxidants on the different mineralization pathways (Van Cappellen et al., 1993). In marine sediments the organic matter is initially decomposed by aerobic respiration. When the oxygen in the interstitial water is depleted, the remainder of the organic matter will be degraded successively by denitrification, manganese reduction, iron reduction, sulfate reduction and finally methanogenesis till all metabolizable organic matter is depleted (Froelich et al., 1979).

A variety of enzymatic reactions involving a variety of organisms take part in the decomposition of sedimentary organic matter. During this decomposition various intermediate compounds are produced. Despite the complexity of the reactions, the main pathways of the degradation of organic matter can be described by standard set of overall reactions (Table 4.2).

Kinetic formulations – mineralization reactions

Organic detritus is composed of many different substrates with different degradability. It is supposed that microbial communities sequentially consume the different organic fractions according to their decreasing reactivity. As a result the overall reactivity of the organic matter decreases with time (Berner, 1980a; Westrich and Berner, 1984). Different models are generally used to describe this decrease in degradability during decomposition (Middelburg, 1989; Boudreau and Ruddick, 1991). In this paper we applied a multi–G type of model (Berner, 1980a; Westrich and Berner, 1984).

The organic matter is divided into three fractions. The "refractory" organic matter is defined as the fraction that is not utilized by microorganisms in the timescale

Table 4.2. Mineralization reactions included in the model. In bold are the components that are modeled. Organic matter is represented by $(CH_2O)_x(NH_3)_y(H_3PO_4)$ where x and y denote the molar *C/P*- and *N/P*-ratios of the organic matter respectively

Aerobic respiration
$(CH_2O)_x(NH_3)_y(H_3PO_4) + xO_2 + yH^+$ $\rightarrow xCO_2 + yNH_4^+ + HPO_4^{2-} + 2H^+ + xH_2O$
Denitrification
$(CH_2O)_x(NH_3)_y(H_3PO_4) + \frac{4}{5}xNO_3^- + (\frac{4}{5}x + y)H^+$ $\rightarrow xCO_2 + yNH_4^+ + \frac{2}{5}xN_2 + HPO_4^{2-} + \frac{7}{5}xH_2O$
Dissimilatory manganese reduction
$(CH_2O)_x(NH_3)_y(H_3PO_4) + 2xMnO_2 + (4x + y)H^+$ $\rightarrow xCO_2 + 2xMn^{2+} + yNH_4^+ + HPO_4^{2-} + 2H^+ + 3xH_2O$
Dissimilatory iron reduction
$(CH_2O)_x(NH_3)_y(H_3PO_4) + 4xFe(OH)_3 + (8x + y)H^+$ $\rightarrow xCO_2 + 4xFe^{2+} + yNH_4^+ + HPO_4^{2-} + 2H^+ + 11xH_2O$
Sulfate reduction
$(CH_2O)_x(NH_3)_y(H_3PO_4) + \frac{1}{2}xSO_4^{2-} + (\frac{1}{2}x + y)H^+$ $\rightarrow xCO_2 + \frac{1}{2}x\Sigma H_2S + yNH_4^+ + HPO_4^{2-} + H^+ + xH_2O$
Methanogenesis
$(CH_2O)_x(NH_3)_y(H_3PO_4) + yH^+$ $\rightarrow \frac{1}{2}xCO_2 + \frac{1}{2}xCH_4 + yNH_4^+ + HPO_4^{2-} + 2H^+$

of early diagenesis. The reactive organic matter is divided in a fast and a slow decaying fraction with different stoichiometry. A Redfield *N/C* ratio (0.1509) is assumed for the fast decaying fraction. The slow decaying organic matter is assumed to be poorer in nitrogen and a *N/C* ratio of 0.105 was derived by model calibration. The result is that the model simulates the increase in *N/C* ratio with depth in the sediment that is observed in coastal, marine and estuarine sediments (Jørgensen, 1983; Klump and Martens, 1987; Burdige, 1991). The first-order degradation constant at 20°C for the fast decaying organic matter is 7.53×10^{-2} d^{-1} (Westrich and Berner, 1984; Boudreau and Ruddick, 1991). For the slow decaying part, a degradation constant of 3.0×10^{-3} d^{-1} was derived by model calibration. The rate constants are corrected for temperature, assuming a Q_{10}-value of 2 (Wells, 1980; Piepenburg et al., 1995). The ratio between the fast and slow decaying organic matter sedimenting on the bottom is dependent on the water depth (Soetaert et al., 1996a), and is included in the model as an input parameter.

It has been well recognized that the rate of metabolic activity of each degradation pathway is not only depending on the reactivity of the organic matter, but also on the availability of the electron acceptor (Rabouille and Gaillard, 1991a; Dhakar and Burdige, 1996). The limitation of oxidants is modeled by a Monod-type hyperbolic limitation function (Boudreau and Westrich, 1984; Soetaert et al., 1996a)

$$Limit = \frac{[EA]}{[EA] + K_m},$$ (4.3)

Table 4.3. Parameter values used in the model simulations. *M*: parameters derived by model calibration; *A*: independent parameters that have been assumed; *D*: independent parameters based on observations

Parameter	Value	Units	Description	
Db_0	3.3×10^{-2}	cm^2 d^{-1}	Bioturbation coefficient in bioturbated layer (0-x_b cm)	M
x_b	1	cm	Thickness of constant bioturbation layer	M
$coeff_{Db}$	1	cm	Coefficient for exponential bioturbation decrease	M
ω	3×10^{-4}	cm d^{-1}	Sedimentation rate	M
PFdet	0.29	-	Part of reactive organic matter that is fast decaying	M
T	5.8	°C	Temperature of the bottom water	D
O_2(bw)	295	μM	Oxygen concentration in the bottom water	D
NO_3(bw)	5	μM	Nitrate concentration in the bottom water	A
NH_3(bw)	0.58	μM	Ammonia concentration in the bottom water	D
Mn(bw)	0	μM	Manganese concentration in the bottom water	A
Fe(bw)	0	μM	Ferrous iron concentration in the bottom water	A
SO_4(bw)	1.604×10^4	μM	Sulfate concentration in the bottom water	A
H_2S(bw)	0	μM	Hydrogen sulfide concentration in the bottom water	A
CH_4(bw)	0	μM	Methane concentration in the bottom water	A
MnO_2-flux	0.01	μmol Mn cm^{-2} d^{-1}	Manganese-oxide flux to the sediment	M
$Fe(OH)_3$-flux	0.028	μmol Fe cm^{-2} d^{-1}	Iron-oxide flux to the sediment	M
FeS-flux	0	μmol FeS cm^{-2} d^{-1}	Iron-monosulfide flux to the sediment	A
FeS_2-flux	0	μmol FeS_2 cm^{-2} d^{-1}	Pyrite flux to the sediment	A
R_{m1}	7.53×10^{-2}	d^{-1}	First order degradation constant fast decaying detritus at 20°C	(1)
R_{m2}	3×10^{-3}	d^{-1}	First order degradation constant slow decaying detritus at 20°C	M
Q_{10}	2	-	Q_{10}-factor organic matter degradation	A
ΣR_{min}	0.5	mmol C cm^{-2} yr^{-1}	Total depth-integrated carbon mineralization rate	M
IrrEnh	2.5	-	Irrigation enhancement factor	M
NH_3-ads	1.3	-	Adsorption coefficient of ammonia	(1)
γ_{TOC1}	0.1509	mol N (mol C)$^{-1}$	N/C ratio of fast decaying detritus	(1)
γ_{TOC2}	0.105	mol N (mol C)$^{-1}$	N/C ratio of slow decaying detritus	M
$K_{in}(O_2$ denit)	10	μM O_2	Half-saturation conc. O_2 inhibition for denitrification	(1)
$K_{in}(O_2)$	8	μM O_2	Half-saturation conc. O_2 inhibition for anoxic mineralization	(2)
$K_{in}(NO_3)$	10	μM NO_3	Half-saturation conc. NO_3 inhibition	(2)
$K_{in}(MnO_2)$	5000	μmol MnO_2 dm^{-3}	Half-saturation conc. MnO_2 inhibition	(2)
$K_{in}(Fe(OH)_3)$	1.25×10^4	μmol $Fe(OH)_3$ dm^{-3}	Half-saturation conc. $Fe(OH)_3$ inhibition	(2)
$K_{in}(SO_4)$	1000	μM SO_4	Half-saturation conc. SO_4 inhibition	(2)
$K_s(O_2)$	3.1	μM O_2	Half-saturation conc. O_2 limitation for oxic mineralization	(1)
K_s(nit)	1	μM O_2	Half-saturation conc. O_2 limitation for nitrification	(1)
$K_s(NO_3)$	30	μM NO_3	Half-saturation conc. NO_3 limitation for nitrification	(1)
$K_s(MnO_2)$	5000	μmol MnO_2 dm^{-3}	Half-saturation conc. MnO_2 limitation for manganese reduction	(2)
$K_s(Fe(OH)_3)$	1.25×10^4	μmol $Fe(OH)_3$ dm^{-3}	Half-saturation conc. $Fe(OH)_3$ limitation for iron reduction	M
$K_s(SO_4)$	1620	μM SO_4	Half-saturation conc. SO_4 limitation for sulfate reduction	(3)
Ks_{FeS}	6.31×10^3	μM	Saturation constant FeS	(4)
k_{nitr}	20	d^{-1}	Rate constant nitrification	(1)
k_{MnO2}	1.37×10^{-2}	μM^{-1} d^{-1}	Rate constant Mn^{2+} oxidation by O_2	(4)
k_{FeO2}	2.938×10^{-1}	μM^{-3} d^{-1}	Rate constant Fe^{2+} oxidation by O_2	(5)
k_{H2SO2}	4.39×10^{-4}	μM^{-1} d^{-1}	Rate constant H_2S oxidation by O_2	(4)
k_{CH4O2}	27.4	μM^{-1} d^{-1}	Rate constant CH_4 oxidation by O_2	(4)
k_{FeSO2}	8.22×10^{-4}	μM^{-1} d^{-1}	Rate constant FeS oxidation by O_2	(4)
k_{PyrO2}	4.38×10^{-4}	μM^{-1} d^{-1}	Rate constant FeS_2 oxidation by O_2	M
k_{FeMn}	8.22×10^{-3}	μM^{-1} d^{-1}	Rate constant Fe^{2+} oxidation by MnO_2	(4)
k_{H2SMn}	5.48×10^{-5}	μM^{-1} d^{-1}	Rate constant H_2S oxidation by MnO_2	(4)
k_{H2Sfe}	1×10^{-7}	μM^{-1} d^{-1}	Rate constant H_2S oxidation by $Fe(OH)_2$	M
k_{CH4SO4}	2.74×10^{-5}	μM^{-1} d^{-1}	Rate constant CH_4 oxidation by SO_4^{2-}	(4)
$k_{FeS,1}$	1	μM^{-1} d^{-1}	Rate constant FeS formation	(4)
$k_{FeS,2}$	2.74×10^{-6}	d^{-1}	Rate constant FeS dissolution	(4)
k_{pyrite}	8.90×10^{-6}	μM^{-1} d^{-1}	Rate constant pyrite formation	(6)

(1) (Soetaert et al., 1996a), (2) (Van Cappellen and Wang, 1995), (3) (Boudreau and Westrich, 1984), (4) (Van Cappellen and Wang, 1996), (5) (Millero et al., 1987), (6) (Rickard, 1997b)

where *[EA]* is the concentration of the limiting electron acceptor and K_m is the half-saturation concentration. The K_m-values used in the model are given in table 4.3. In addition, the presence of oxidants may inhibit the oxidation of carbon by energetically less powerful electron acceptors. This inhibition is described by a reciprocal hyperbolic function (Van Cappellen et al., 1993; Soetaert et al., 1996a)

$$Inhib = \left(1 - \frac{[\,IN\,]}{[\,IN\,] + K_{in}} \right),$$ (4.4)

where *[IN]* is the concentration of the inhibiting oxidant and K_{in} is the inhibition constant. The inhibition constants used in the model have been derived from literature and are summarized in table 4.3. Mineralization proceeds up till all degradable carbon is removed. The degradation rates of the individual respiratory pathways are finally re-scaled to ensure that sum of the individual rates equals the total degradation rate (Soetaert et al., 1996a). As such the degradation rate of the organic matter is independent of the various oxidants and the organic carbon profile can be solved independently of the distribution of the other components in the sediment (Soetaert et al., 1996a). The result of the use of limitation and inhibition functions is that the model represents the spatial sequence of the successive degradation pathways as observed in marine sediment. The extent of vertical overlap between the various mineralization processes can be adjusted with the parameters K_m and K_{in}.

Secondary reactions

The mineralization reactions of the organic matter produce a variety of reduced pore-water species such as NH_4, Mn, Fe, H_2S and CH_4. These reduced substances diffuse upward in the sediment column, where they are re-oxidized in a more oxidized environment. When sulfide produced by sulfate reduction meets ferrous iron it can form iron monosulfide (*FeS*), which can again react with sulfide to form pyrite (FeS_2). The secondary reactions incorporated in the model are given in table 4.4. A description of the various reactions can be found in Boudreau (1996a) and Van Cappellen and Wang (1996) and references therein.

Kinetic formulations – secondary reactions

The kinetics of most secondary redox reactions in the sediment is not fully understood. Microorganisms mediate most, if not all the reactions and Monod-type kinetics seems to be appropriate. Nitrification is described by Monod-type kinetics and it is assumed that the ammonium produced by aerobic mineralization is directly converted into nitrate (Soetaert et al., 1996a)

$$R_{nitr} = k_{nitr} \cdot [\,NH_3\,] \cdot \frac{[O_2\,]}{[O_2\,] + K_s(\,nit\,)} + N_{coupled}\,,$$ (4.5)

where R_{nitr} is the rate of nitrification (µM d^{-1}), k_{nitr} is the rate constant for nitrification (d^{-1}), $K_s(nit)$ is the half saturation constant (µM) and $N_{coupled}$ is the rate of nitrification coupled to the oxic degradation of organic matter (µM d^{-1}).

For most other re-oxidation reactions we followed Van Cappellen and Wang (1996), who used bi-molecular reaction rate laws to describe the reaction kinetics. Bi-molecular kinetics approaches Monod-kinetics when the concentrations of both electron acceptor and electron donor are low. In natural sediments the secondary redox reactions are often confined to areas of limiting concentrations (Berner, 1980b; Van Cappellen and Wang, 1996). Reaction rates have then first-order dependence on the electron acceptor and donor.

$$R = k \cdot [\,EA\,] \cdot [\,ED\,]\,,$$ (4.6)

Table 4.4. Secondary reactions included in the model. In bold are the modeled components

Re-oxidation reactions with oxygen as oxidant
$NH_4^+ + 2O_2 + 2HCO_3^- \rightarrow NO_3^- + 2CO_2 + 3H_2O$
$Mn^{2+} + \frac{1}{2}O_2 + 2HCO_3^- \rightarrow MnO_2 + 2CO_2 + H_2O$
$Fe^{2+} + \frac{1}{4}O_2 + 2HCO_3^- + \frac{1}{2}H_2O \rightarrow Fe(OH)_3 + 2CO_2$
$\Sigma H_2S + 2O_2 + 2HCO_3^- \rightarrow SO_4^{2-} + 2CO_2 + 2H_2O$
$FeS + 2O_2 \rightarrow Fe^{2+} + SO_4^{2-}$
$FeS_2 + \frac{7}{2}O_2 + H_2O \rightarrow Fe^{2+} + 2SO_4^{2-} + 2H^+$
$CH_4 + 2O_2 \rightarrow CO_2 + 2H_2O$
Re-oxidation with Mn-Fe oxides as oxidant
$MnO_2 + 2Fe^{2+} + HCO_3^- + 2H_2O \rightarrow Mn^{2+} + 2Fe(OH)_3 + 2CO_2$
$MnO_2 + \Sigma H_2S + 2CO_2 \rightarrow Mn^{2+} + S^0 + 2HCO_3^-$
$2Fe(OH)_3 + \Sigma H_2S + 4CO_2 \rightarrow 2Fe^{2+} + S^0 + 4HCO_3^- + 2H_2O$
Re-oxidation reactions with sulfate as oxidant
$CH_4 + SO_4^{2-} + CO_2 \rightarrow 2HCO_3^- + \Sigma H_2S$
Precipitation reactions
$Fe^{2+} + HS^- + HCO_3^- \leftrightarrow FeS + CO_2 + H_2O$
$FeS + H_2S \rightarrow FeS_2 + H_2$

where R is the reaction rate (μM d^{-1}), k is the reaction rate constant (μM^{-1} d^{-1}) and [EA] and [ED] are the concentrations of the electron acceptor and electron donor respectively (μM). The rate constants were derived from Van Cappellen and Wang (1996) who give a compilation of model-derived and literature data (Table 4.3). Unlike Van Cappellen and Wang (1996), the re-oxidation of ferrous iron with oxygen is dependent on *pH* and is described in this model by (Millero et al., 1987):

$$R = k_{FeO2} \cdot [O_2] \cdot [Fe^{2+}] \cdot [OH^-]^2 , \tag{4.7}$$

where k_{FeO2} is the reaction rate constant (μM^{-3} d^{-1}).

The precipitation of *FeS* from Fe^{2+} and (HS^-) is a reversible reaction. The variable Ω_{FeS} gives the degree of saturation of the pore water with Fe^{2+} and HS^-:

$$\Omega_{FeS} = \frac{[Fe^{2+}] \cdot [HS^-]}{\{H^+\} \cdot Ks_{FeS}} , \tag{4.8}$$

where Ks_{FeS} is the apparent solubility product. When $\Omega_{FeS} > 1$, precipitation takes place at a rate of

$$\frac{dFeS}{dt} = k_{FeS,1} \cdot (\Omega - 1) \tag{4.9}$$

and when $\Omega_{FeS} < 1$, dissolution of *FeS* takes place at a rate of

$$\frac{dFeS}{dt} = -k_{FeS,2} \cdot [\,FeS\,] \cdot (\,1 - \Omega\,), \tag{4.10}$$

where $k_{FeS,1}$ and $k_{FeS,2}$ are forward and backward first-order rate constants respectively.

The formation of pyrite is described by bi-molecular rate kinetics (Rickard, 1997a, Rickard, 1997b).

$$\frac{dFeS_2}{dt} = k_{Pyrite} \cdot [\,FeS\,] \cdot [\,H_2S\,], \tag{4.11}$$

where k_{Pyrite} is the first order rate constant.

Transport processes

Molecular diffusion

Molecular diffusion is important for the dissolved pore water components. The free-solution diffusion coefficient (D^T) (units of cm^2 s^{-1}) for electrolytes at the ambient temperature t (°C) is calculated from the zero-degree coefficient D^0:

$$D^T = D^0 + at, \tag{4.12}$$

where a is an ion-specific coefficient. The regression parameters D^0 and a for the electrolytes included in the model are given in table 4.5.

Table 4.5. Linear regression coefficients free-solution diffusion coefficient D^T (10^{-6} cm^2 s^{-1}) versus temperature t (°C). Adapted from Boudreau (1997) based on data from Li and Gregory (1974)

Cations	D_0 (10^{-6} cm^2 s^{-1})	a (10^{-6} cm^2 s^{-1} °C^{-1})	Anions	D^0 (10^{-6} cm^2 s^{-1})	a (10^{-6} cm^2 s^{-1} °C^{-1})
NH_4^+	9.50	0.413	NO_3^-	9.50	0.388
Fe^{2+}	3.31	0.150	HS^-	10.4	0.273
Mn^{2+}	3.43	0.144	SO_4^{2-}	4.88	0.232

For the non-electrolyte CH_4, the free solution diffusion coefficient is described by an empirical correlation developed by Wilke and Chang (1955) and corrected by Hayduk and Laudie (1974)

$$D^T = 4.72 \cdot 10^{-9} \cdot \frac{T}{\mu V_b^{0.6}}, \tag{4.13}$$

where D^T is the free-solution diffusion coefficient (cm^2 s^{-1}), T is the absolute temperature (°K), μ is the dynamic viscosity in units of poise (g cm^{-1} s^{-1}) and V_b is 37.7 cm^3 mol^{-1} for CH_4 (Hayduk and Laudie, 1974).

Finally for O_2, the following empirical relation is used to calculate D^T (Boudreau, 1997)

$$D^T = (\ 0.2604 + 0.006383 \cdot (\ \frac{T}{\mu \cdot 0.01}\ ))\cdot 10^{-5}\ , \tag{4.14}$$

where T is the absolute temperature (°K) and μ is the dynamic viscosity in units of poise (g cm^{-1} s^{-1}).

The diffusion coefficient of a dissolved substance in the sediment (D_S^T) is lower than its free-solution diffusion coefficient in water (D^T) because of the convoluted path molecules must follow to circumvent the sediment particles. According to Berner (1980b), D_S^T is related to D^T by:

$$D_S^T = \frac{D^T}{\theta^2}\ , \tag{4.15}$$

where θ is the tortuosity of the sediment. The tortuosity is related to the sediment porosity (Boudreau, 1996b). In this model we used Archie's Law with the empirical coefficient m set to 3 (Ullman and Aller, 1982; Reimers et al., 1992). The effective diffusion coefficient of a dissolved substance in the sediment is then calculated as (Soetaert et al., 1996a)

$$D_S^T = D^T \cdot \phi^2 \tag{4.16}$$

Advection

Advection is the process of material transport due to deposition of new material at the sediment surface (Berner, 1980b). As a result of this deposition the sediment will be compacted. In general compaction results in an increasing advection rate with sediment depth for solute substances and a decrease in advection rate with depth for solids (Rabouille and Gaillard, 1991a). We neglected the effect of compaction and assumed the rate of advection to be equal to the sedimentation rate for all components at all sediment depths.

Sediment compaction was not explicitly modeled, but the result of compaction, i.e. an exponential decrease of porosity with sediment depth was imposed (Berner, 1980b; Rabouille and Gaillard, 1991a; Rabouille and Gaillard, 1991b; Soetaert et al., 1996a):

$$\phi_x = \phi_\infty + (\ \phi_0 - \phi_\infty\ )\cdot e^{-\tau \cdot x}\ , \tag{4.17}$$

where ϕ_0 and ϕ_∞ are the porosity at the sediment water interface and at infinitive depth respectively and τ is the attenuation coefficient (cm^{-1}). For station 9, the parameters ϕ_0 (= 0.95), ϕ_∞ (= 0.73) and τ (=0.23 cm^{-1}) were derived by least squares curve fitting (Figure 4.3).

Bioturbation

Bioturbation, the process of sediment displacement by the activity of benthic organisms, is modeled as a random diffusion-like process (Boudreau, 1986). It is assumed to be constant in the upper part of the sediment ($0 \leq x \leq x_b$) and decreasing exponentially at depth $> x_b$ (Figure 4.4):
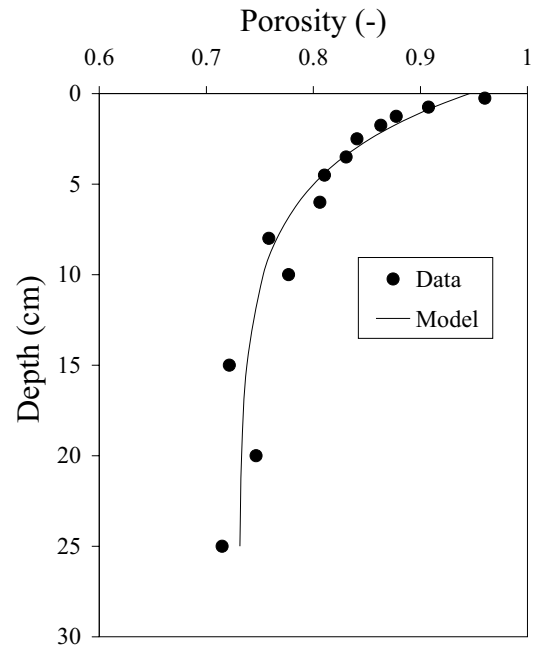
Figure 4.3. Sediment porosity versus depth. The solid line represents the exponential curve that was fitted through the data
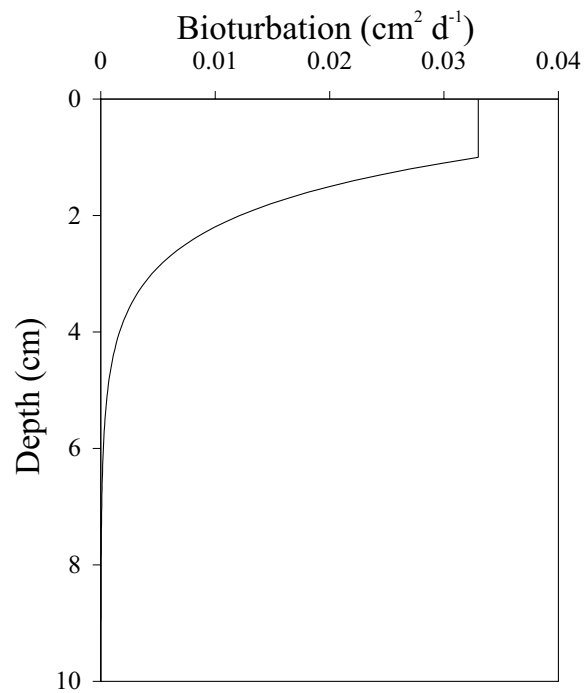

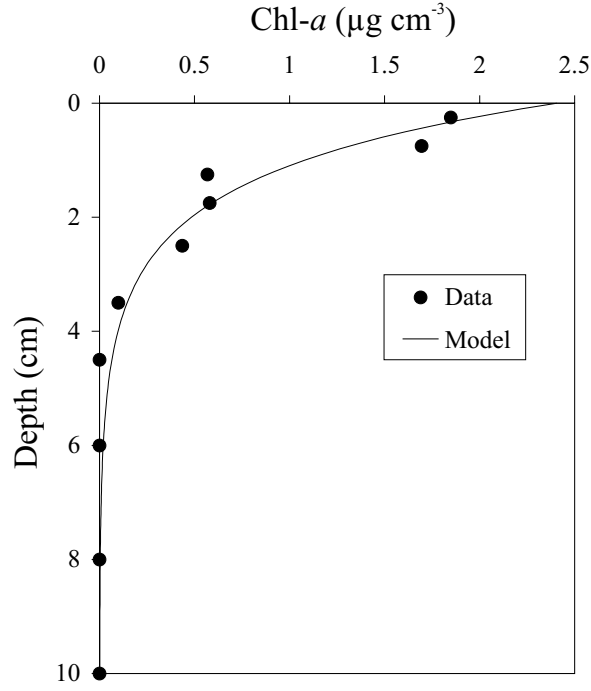**Figure 4.4.** Imposed bioturbation profile

Figure 4.5. Chlorophyll *a* (µg cm^{-3} bulk sediment) versus depth. The solid line was derived by curve fitting of a simple advection–diffusion–reaction equation through the data

$$Db_x = \begin{cases} Db_0 & (\ x \le x_b\ ) \\ Db_0 \cdot e^{-\frac{x-x_b}{coeffDb}} & (\ x > x_b\ ) \end{cases}, \tag{4.18}$$

where Db_x the rate of bioturbation at depth x (cm^2 d^{-1}) and *coeffDb* is the coefficient for exponential bioturbation decrease (cm).

The rate of bioturbation has been derived by least squares curve-fitting of the depth profiles of chlorophyll *a* in the sediment (Figure 4.5). Assuming steady-state conditions, constant porosity, no compaction and first order degradation, the chlorophyll *a* kinetics can be described by (Sun et al., 1994; Soetaert et al., 1996c; Boon and Duineveld, 1998)

$$\frac{\partial C}{\partial t} = Db_0 \cdot \left(\frac{\partial^2 C}{\partial x^2}\right) - \omega\left(\frac{\partial C}{\partial x}\right) - k \cdot C, \tag{4.19}$$

where C is the chlorophyll *a* concentration (in units of µg dm^{-3} bulk sediment), ω is the advection rate (cm d^{-1}) and k is the first order degradation rate of chlorophyll *a* (d^{-1}). Based on cesium data from Curtis & Broadway (1992) the advection rate (ω) on the continental shelf of the Black Sea has been estimated to be typically lower than 2.7×10^{-3} cm d^{-1} (i.e. 1 cm yr^{-1}). The first-order degradation constant (k) for chlorophyll *a* is assumed to range between 0.02 and 0.04 d^{-1} and depends on temperature (Sun et al., 1991). With no advection ($\omega = 0$), the calculated bioturbation ranged between $3.1 \times 10^{-2} - 6.2 \times 10^{-2}$ cm^2 d^{-1}. An advection rate of 2.7×10^{-3} cm d^{-1}

resulted in a slight decrease of derived bioturbation coefficients (2.8×10^{-2} – 5.9×10^{-2} cm^2 d^{-1}). It should be noticed that selective feeding by organisms might result in differences in bioturbation efficiencies with labile organic mater being mixed at a higher rate than more refractory organic matter and inorganic particles (Smith et al., 1993; Soetaert et al., 1998).

Bio-irrigation

Bio-irrigation is the result of construction of tubes by benthic organisms and their ventilation, which causes enhanced exchange of interstitial water with the overlying water (Aller, 1988; Aller and Aller, 1992). As a result the apparent diffusion coefficient in the sediment is increased. In the model we applied a diffusion enhancement factor (*IrrEnh*) of 2.5 for station 9. The apparent sediment diffusion coefficient $Dsed_x$ is calculated from the sediment diffusion coefficient D_S^T multiplied by *IrrEnh*. The irrigation enhancement factor is maximum in the layer of maximum bioturbation ($0 \leq x \leq x_b$) and then decreases exponentially to D_S^T at infinite depth:

$$Dsed_x = \begin{cases} IrrEnh \cdot D_S^T & (x \leq x_b) \\ D_S^T \cdot \left(1 + (IrrEnh-1) \cdot e^{-\frac{(x-x_b)}{coeffDb}}\right) & (x > x_b) \end{cases} \qquad (4.20)$$

Numerical methodology

Since the differential equations in this model are non-linear and highly coupled, and because of the use of depth-variable profiles for porosity, bioturbation and *pH*, the system of differential equations can only be solved numerically. The sediment column is divided into *n* separate layers. The thickness of the first sediment layer (Δx_{sw}) is 1 mm. (Soetaert et al., 1996a). The thickness of the subsequent layers (Δx_i) increases exponentially with depth in the sediment:

$$\Delta x_i = \Delta x_{sw} \cdot \lambda^{i-1}, \qquad (4.21)$$

where λ is the coefficient for the exponential increase in sediment thickness.

We applied the weighted finite differencing method of Fiadeiro and Veronis (1977) to describe the partial differential equations of the solid fractions numerically (Soetaert et al., 1996a). This scheme is appropriate when bioturbation is a function of depth, as is the case in this model. In the bioturbation area, diffusive-like processes will dominate the transport of the solid components and central differencing will be stable and second-order accurate (Boudreau, 1997). At greater sediment depth, advection gradually becomes the dominant transport process for the solid phase components. The central difference scheme is not stable anymore in this area and a switch to backward differences is required. The parameter σ describes this gradual switch from backward to central differencing:

$$\sigma = \frac{1}{tanh(Pe_h)} - \frac{1}{Pe_h}, \qquad (4.22)$$

where Pe_h is one-half of the cell Peclet number (Boudreau, 1996a):

$$Pe_h = \frac{\omega \cdot \Delta x}{2 \cdot Db_x} \tag{4.23}$$

When $\sigma = 0$, diffusive mixing dominates and a central differences scheme is used. When $\sigma = 1$ advective transport processes dominate the transport and a backward differences scheme is used. For dissolved components, diffusive transport always dominates advective transport and is therefore described in a central differencing scheme. Both these numerical schemes can be used for unequally spaced grids and the mass budget is fully closed.

At steady state, the rates of change (dC/dt) must equal zero for all 14 state variables in every compartment. The $14n$ coupled partial differential equations are solved iteratively with the Newton-Rhapson method (Press et al., 1994) starting from imposed initial depth profiles for all variables. When the model failed to reach steady state after 20 iterations, the iteration procedure is restarted with a new set of initial profiles. Since other constituents do not influence the two carbon fractions they can be solved separately. After the carbon profiles are at steady state, the other components are solved with a reduced number of compartments, since their concentrations will not change in the deepest compartments where all the labile carbon has disappeared. This saves computing time. Dynamic simulations were performed using Euler integration with a time step of 10 seconds to avoid numerical instability (Press et al., 1994).

Application of the model

Steady state simulation

Our model is rather simplistic in some respects (e.g. *pH*–profile imposed, number of processes included, bi-molecular rate laws), yet already contains > 50 parameters (Table 4.3). Most parameters were set *a priori*, based on literature information, field measurements (indicated by D) or estimations (indicated by A). The remaining parameters (indicated by M) were obtained by fitting the model profiles to the observations. The performance of the model is demonstrated with a steady state run for station 9 (Figure 4.6). During the fitting procedure, the values were allowed to vary within predetermined ranges. The values of the parameters ΣR_{min}, pFdet, R_{m2}, ω, Db_0, x_b and $coeff_{Db}$ were determined *a priori* on the observed TOC–profile. A depth-integrated rate of carbon mineralization (ΣR_{min}) of 0.33 – 0.39 mmol C cm^{-2} yr^{-1} was calculated from the Sediment Community Oxygen Consumption (SCOC) obtained by deck incubation as described by Wijsman et al. (1999). This value was slightly lower than the value obtained by the model (0.5 mmol C cm^{-2} yr^{-1}, Table 4.3). Parameters MnO_2-flux, $Fe(OH)_3$-flux, $K_s(Fe(OH)_3)$ and k_{H2SMn} were subsequently derived from the observed FeS, FeS_2 and Mn^{2+} profiles. And finally the values of *IrrEnh* and γ_{TOC2} were derived from the NH_4^+ and the Mn^{2+} profiles.

The model failed to describe the high values measured near the sediment surface, but gave a reasonable fit at depths > 2 cm. The model reasonably describes both the depth as well as the height of the subsurface peak of FeS. Also the pyrite concentration at depth is in the same range as the field observations. The model
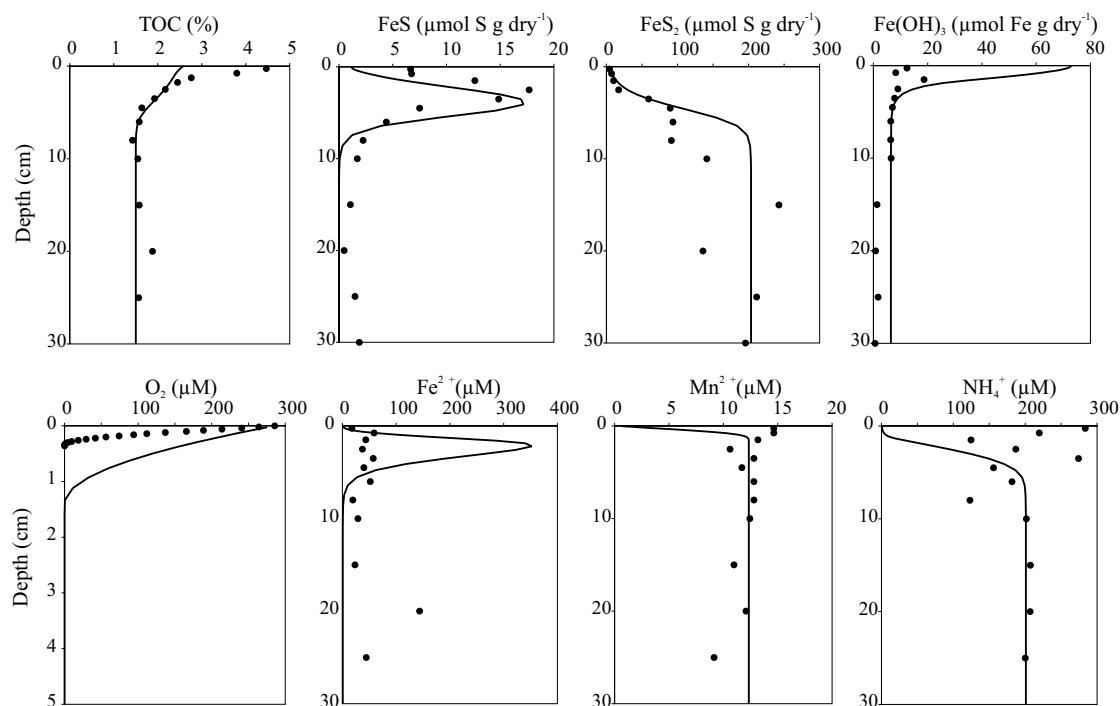
Figure 4.6. Depth distributions of the solid species: total organic carbon (TOC, %), iron monosulfide (*FeS*, μmol *S* g dry^{-1}), pyrite (*FeS$_2$*, μmol *S* g dry^{-1}) and iron oxides (*Fe(OH)$_3$*, μmol *Fe* g dry^{-1}) and the pore water components: oxygen (*O$_2$*, μM), ferrous iron (*Fe^{2+}*, μM), manganese (*Mn^{2+}*, μM) and ammonium (*NH$_4^+$*, μM). The dots indicate the measured data for station 9 and the solid lines indicate the model results of the steady state simulation. Note the different depth scale for oxygen

predicts that all *FeS* has disappeared at depths > 10 cm. However small amounts of *FeS* are still present, indicating either that *FeS* is still being formed at these depths or that the conversion rate to pyrite is slower than predicted. The burial of pyrite can be taken as a measure for the total biologically reactive *Fe(OH)$_3$* flux to the sediment when corrected for the flux of *Fe^{2+}* out of the sediment. The *Fe^{2+}*-flux out of the sediment was low (7.48×10^{-3} μmol *Fe* cm^{-2} d^{-1}) compared to the *Fe(OH)$_3$*-flux (2.8×10^{-2} μmol *Fe* cm^{-2} d^{-1}) into the sediment. The concentration of *Fe(OH)$_3$* in the surface sediment layer is significantly overestimated by the model. The build-up of *Fe(OH)$_3$* is due to re-oxidation of *Fe^{2+}* with oxygen. *Fe(OH)$_3$*-concentrations at a depth > 15 cm are lower than predicted because of non-steady state input of iron-oxides or iron reduction at depth due to variable reactivities of the iron-oxide. Oxygen penetration calculated by the steady state model is much too deep compared to the micro-electrode recordings, indicating a higher consumption rate of oxygen. The subsurface peak of *Fe^{2+}* predicted by the model is not observed. The predicted iron peak is due to a relative thin layer of iron reduction. Iron that diffuses upward will be re-oxidized with oxygen or *MnO$_2$* and that diffusing downward will react with *H$_2$S* to form *FeS*. There is no adsorption of iron to sediment particles (Van Cappellen and Wang, 1996) nor iron carbonate formation (Berner, 1980b; Aller et al., 1986) with the result that iron liberation is likely overestimated. Predicted concentrations of dissolved manganese are consistent with field observations. However, the decrease near the sediment water interface as calculated by the model was not observed. The ammonium concentration at depths > 10 cm is well reproduced, but again deviations

occur near the sediment surface. Observed sulfide concentrations were always below the detection limit (< 1 µM), yet the model predicts hydrogen sulfide up to 560 µM at depth. This is probably caused by the exhaustion of Fe^{2+} to trap the hydrogen sulfide. Iron from the pools of $FeCO_3$ or Fe^{2+} adsorbed to sediment particles may act as a buffer and maintain a considerable amount of Fe^{2+} at depth.

Dynamic simulation

For most constituents, the results of the steady state model deviate from the observed profiles near the sediment water interface. Especially the modeled profiles of TOC, iron oxides, oxygen and ammonium seem to fail near the sediment water interface. Although sampling of pore water in the upper sediment layers is difficult and subject to considerable error, non-steady state sedimentation could also change the concentrations in the top layer of the sediment. Our observations were done in May, i.e after the spring bloom, and it might well be possible that the sediment is still recovering from a pulse deposition of fresh organic matter. A steady state model can not cope with such temporal variability. With a dynamic simulation, we tested whether a temporal change in the organic matter flux from the spring bloom just before we sampled the sediment could have caused some of the discrepancies. Starting from the steady state situation we forced a sinusoidal peak of degradable organic matter (ΣR_{min}) to the sediment (Figure 4.7, upper panel). All other parameters and forcings were kept the same as during the steady state simulation. The period of the pulse was 15 days, and a maximum of 17.4 µmol C cm^{-2} d^{-1} was reached after 7.5 days. The total carbon flux to the sediment on a yearly basis increased about 25% due to this pulse flux.

The depth profiles of TOC, oxygen, iron and ammonium are plotted for t=0 (steady state situation), t=15 (directly after the pulse) and t=60 days in figure 4.7, lower panels. Especially the profiles of TOC and oxygen after the pulse (i.e. at t=15 days) are notably better than the profiles from the steady state run. Iron reacts very quickly on the pulse of organic matter, while the reaction of the ammonium profiles is more retarded. It will be clear that the pore water concentrations near the sediment water interface are vulnerable to non-steady state conditions. This puts severe restrictions on the use of steady state models to systems subject to seasonal deposition.

Mineralization pathways as a function of carbon loading

Organic matter, either derived from the water column by sedimentation or from the benthic primary production is the ultimate energy source for the early diagenetic processes in the sediment. In deep-sea stations where the organic matter flux to the sediment is generally low, oxic mineralization and denitrification are important pathways for the degradation of the organic matter in the sediment (Soetaert et al., 1996b). With an increase of the total rate of mineralization in the sediment, anoxic degradation pathways, including iron and sulfate reduction become more important (Canfield et al., 1993b).

To investigate the effect of the carbon loading on the relative importance of mineralization pathways, we performed 300 steady state simulations, with all parameters identical to that of the steady state simulation (Table 4.3). The total
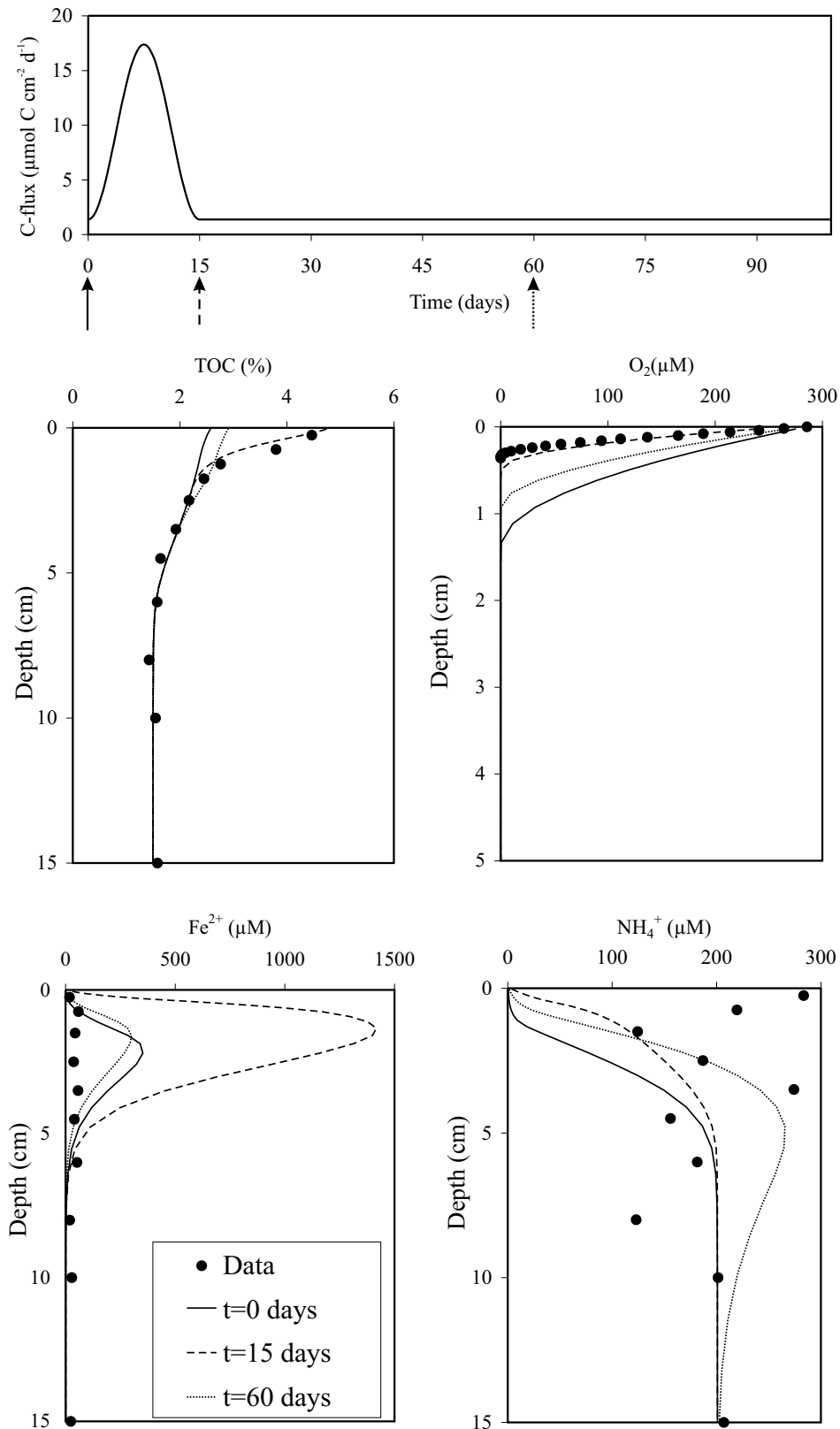
Figure 4.7. Results of a dynamic simulation with the model. The upper panel shows the sinusoidal pulse flux of organic matter to the sediment that was forced to the model. Maximum flux is at day 7.5 and the period is 15 days. The lower panels show the depth distributions in the sediment of total organic carbon (TOC, %) and the dissolved components oxygen (O_2, µM), ferrous iron (Fe^{2+}, µM) and ammonium (NH_4^+, µM). The lines represents the results of the dynamic simulation at t=0 days (solid line), t=15 days (dashed line) and t=60 days (dotted line)
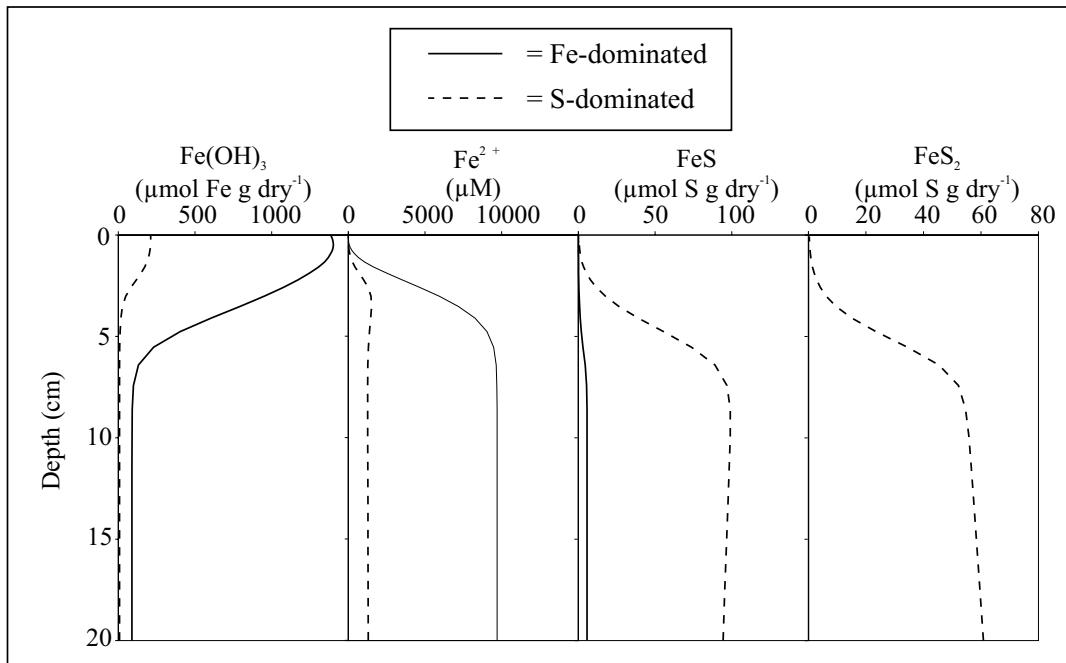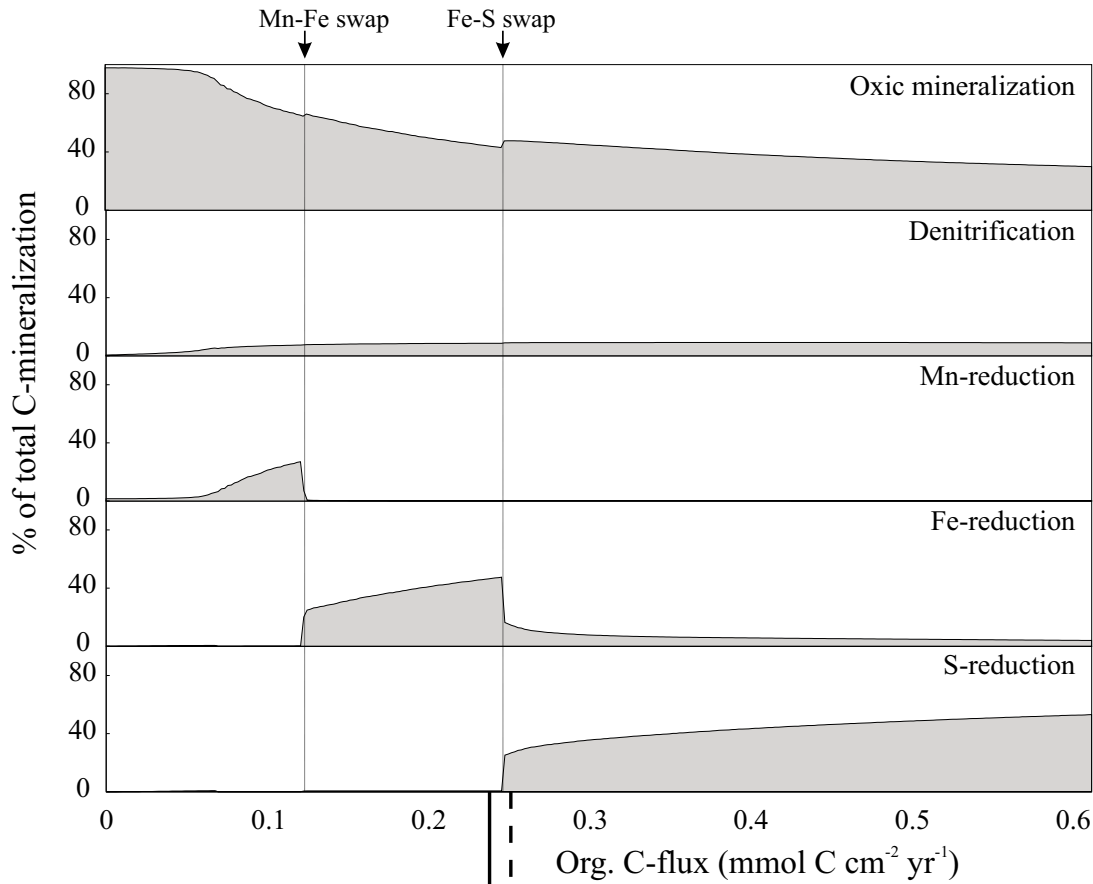
Figure 4.8. The upper panel represents the effect of the organic matter flux to the sediment on the relative importance (%) of the various mineralization pathways. The *Mn-Fe* and *Fe-S* swaps are indicated. The lower panel shows the depth distributions of iron oxides (*Fe(OH)$_3$*, μmol *Fe* g dry^{-1}), ferrous iron (*Fe^{2+}*, μM), iron monosulfide (*FeS*, μmol *S* g dry^{-1}) and pyrite (*FeS$_2$*, μmol *S* g dry^{-1}) for a *Fe*-dominated situation (Org. *C* flux = 0.24 mmol *C* cm^{-2} yr^{-1}, solid line) and a *S*-dominated situation (Org. *C* flux = 0.25 mmol *C* cm^{-2} yr^{-1}, dashed line)

degradable organic carbon flux to the sediment (ΣR_{min}) was varied by means Latin hypercube sampling technique (Press et al., 1994) between 0 and 0.6 mmol C cm^{-2} yr^{-1}. The relative contribution of each degradation pathway as a function of total carbon mineralization is shown in figure 4.8, upper panel. Methanogenesis always accounted for less than 4% of the total carbon mineralization and is therefore not plotted. Oxic mineralization is the dominant degradation pathway at low carbon fluxes. With increasing carbon loading, suboxic and anoxic degradation pathways become more important. Denitrification then accounts for 8 to 10% of the total carbon degradation, consistent with an extensive Monte Carlo sensitivity analysis by Middelburg et al. (1996b). Carbon degradation by manganese reduction is only of importance at mineralization rates between 0.05 and 0.12 mmol C cm^{-2} yr^{-1}. At a mineralization rate of 0.12 mmol C cm^{-2} yr^{-1} there is an abrupt change from manganese reduction to iron reduction (indicated by *Mn-Fe* swap). At this carbon loading, manganese oxides become exhausted in the sediments and iron reduction will occur. Ferrous iron produced by iron reduction diffuses upward and consumes manganese oxides, which are therefore not anymore available for organic matter degradation. This has in turn a positive feedback on the rate of iron reduction. Accordingly manganese reduction changes abruptly from reduction coupled to organic matter oxidation to reduction coupled to ferrous iron oxidation. A similar situation is observed at a degradation rate between 0.24 and 0.25 mmol C cm^{-2} yr^{-1} where an abrupt change occurs from iron reduction to sulfate reduction (indicated by *Fe-S* swap).

The effect of the *Fe-S* swap on the steady state profiles is illustrated in the lower panel of figure 4.8. The solid and broken lines are steady state profiles for a *Fe*-dominated situation (Org. C flux = 0.24 mmol C cm^{-2} yr^{-1}) and a S-dominated situation (Org. C flux = 0.25 mmol C cm^{-2} yr^{-1}), respectively. In the *Fe*-dominated situation, *Fe(OH)$_3$* and the *Fe^{2+}* reach extreme high concentrations, free sulfide is not observed since all the produced sulfide is directly converted into iron monosulfide and pyrite is not produced. In the *S*-dominated situation, concentrations of *Fe^{2+}* and *Fe(OH)$_3$* are much lower, free sulfide is observed in the pore water (up to 40 µM) and significant quantities of iron monosulfide and pyrite are produced.

The steady state budgets for iron and sulfur before and after the *Fe-S* swap are given in figure 4.9. Fluxes and depth-integrated reaction rates higher than 10 nmol cm^{-2} d^{-1} have been accentuated. Just before the swap (*Fe*-dominated situation), no free sulfide is observed in the pore water because the sulfide generated is efficiently trapped by abundant iron. At a slightly higher mineralization rate (*S*-dominated situation), the rate of iron monosulfide production is increased and a substantial part of reduced iron is trapped into *FeS* and *FeS$_2$* and will therefore not be re-oxidized to *Fe(OH)$_3$*. Consequently less iron is available for organic matter mineralization and more labile carbon becomes available for sulfate reducers, hence the rate of sulfate reduction is enhanced.

Ferrous iron, produced by the reduction of iron (oxy)hydroxides coupled to carbon oxidation can be re-oxidized in the less reducing layer with oxygen or manganese oxide. Iron atoms can thus cycle many times through their oxidized and reduced state before ultimate removal to depth in the sediment or escape to the water column (Canfield et al., 1993b). The cycling efficiency of iron, a measure for the average number of cycles in which *Fe* is involved is defined as:
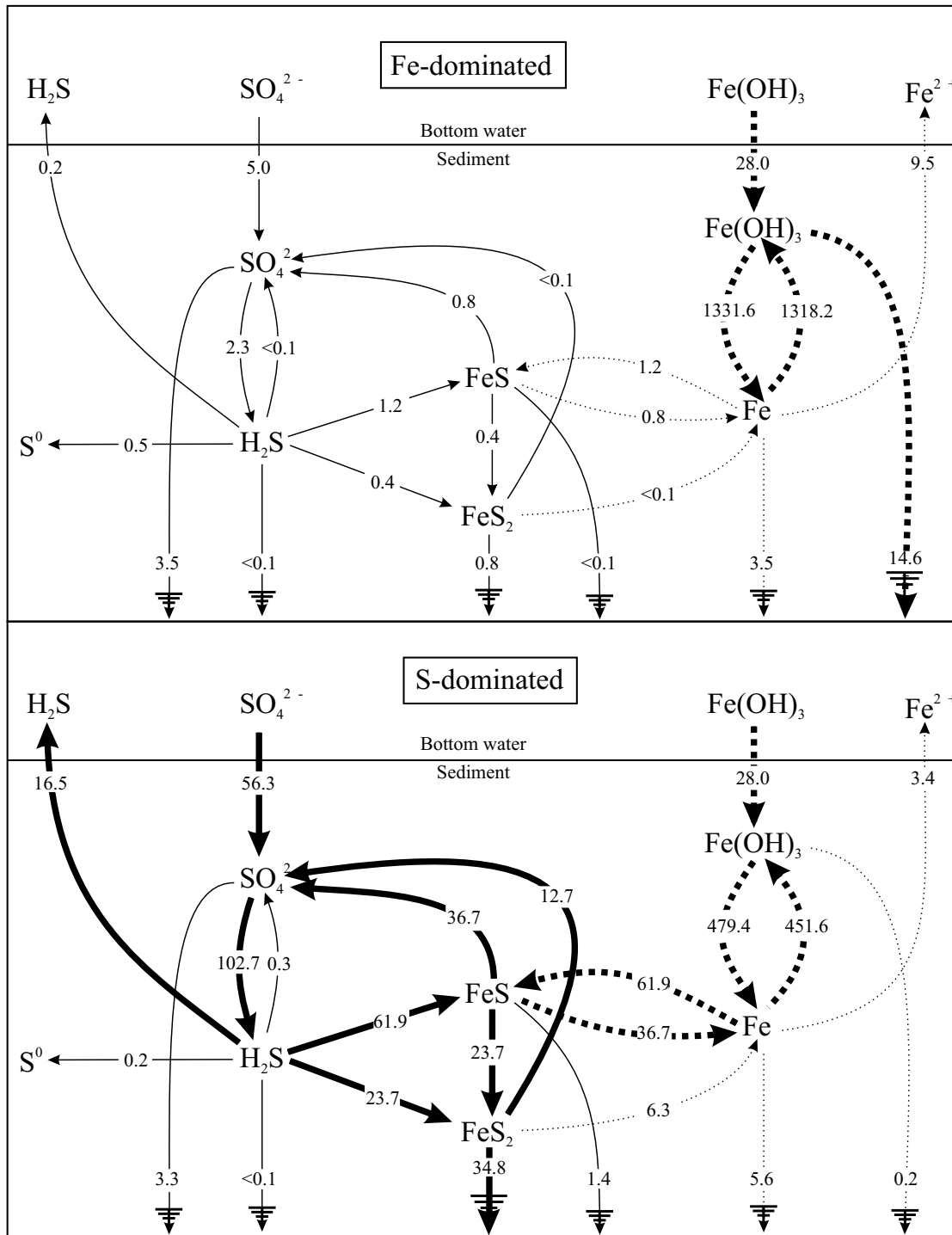
$$E = \frac{R_{red}}{J + R_{red}},$$
(4.24)

Figure 4.9. Schematic representation of the cycling of iron (dashed arrows) and sulfur (solid arrows). The depth-integrated reaction rates and fluxes are indicated in nmol cm^{-2} d^{-1}. Fluxes higher than 10 nmol cm^{-2} d^{-1} have been accentuated. The upper panel represents the situation for a carbon flux of 0.24 (*Fe*-dominated) and the lower panel for carbon flux of 0.25 mmol C cm^{-2} yr^{-1} (*S*-dominated)

where R_{red} is the depth integrated rate of iron reduction and J is the flux of *Fe(OH)$_3$* to the sediment (Wang and Van Cappellen, 1996). The cycling efficiency may vary between 0 (no iron reduction) and 1 (no burial of *Fe*-atoms in the sediment and no

efflux of Fe^{2+} to the water column). A value between 0.5 and 1 indicates active redox recycling of iron in the sediment (Wang and Van Cappellen, 1996). The higher the cycling efficiency, the more important the recycling of Fe-atoms in the sediment. Just before the swap from a iron-dominated system to a sulfur-dominated system, the cycling efficiency of iron was 0.98, indicating that a Fe-atom is on average 54 times recycled. Just after the swap the cycling efficiency decreased to 0.94, which means that each Fe-atom is recycled only 16 times because they become fixed as iron sulfides.

Conclusions

Organic matter mineralization in sediments from the northwestern continental shelf of the Black Sea induces metal oxide and sulfate reduction. These processes have resulted in the transformation of iron oxides into pyrite. A simple diagenetic model including only 14 state variables reproduces the main features observed in these sediments. It was not possible to conceal all observations: i.e. observed dissolved iron concentrations were significantly higher than modeled ones and modeled sulfide concentrations were higher than those observed. Moreover, steady-state predictions in the near surface layer of the sediment deviated from those observed for oxygen, ammonium, ferrous iron, manganese and total organic carbon. Dynamic simulations revealed that the upper few centimeters of the sediments were still recovering from the spring bloom. Exploration of the model over a range of carbon loadings resulted in the identification of two abrupt changes in mineralization pathways, namely from manganese-oxide based to iron- oxide based respiration and from iron-oxide based to sulfate based respiration. These sudden changes have also consequences for buffer capacity of these sediments towards sulfide and phosphorus release.